

See discussions, stats, and author profiles for this publication at: <https://www.researchgate.net/publication/236652689>

# Efficient Orthogonal Integration of the Bacteriophage $\phi 29$ DNA–Portal Connector Protein in Engineered Lipid Bilayers

ARTICLE in ACS SYNTHETIC BIOLOGY · SEPTEMBER 2012

Impact Factor: 4.98 · DOI: 10.1021/sb3000063 · Source: PubMed

CITATION

1

READS

55

## 7 AUTHORS, INCLUDING:



**Lara H. Moleiro**

Complutense University of Madrid

9 PUBLICATIONS 42 CITATIONS

SEE PROFILE



**Marisela Velez**

Spanish National Research Council

75 PUBLICATIONS 1,797 CITATIONS

SEE PROFILE



**José L Carrascosa**

Spanish National Research Council

290 PUBLICATIONS 7,899 CITATIONS

SEE PROFILE



**Francisco Monroy**

Complutense University of Madrid

103 PUBLICATIONS 1,593 CITATIONS

SEE PROFILE

# Efficient Orthogonal Integration of the Bacteriophage $\phi$ 29 DNA-Portal Connector Protein in Engineered Lipid Bilayers

Lara H. Moleiro,<sup>†</sup> Iván López-Montero,<sup>†</sup> Ileana Márquez,<sup>‡</sup> Sonia Moreno,<sup>§,#</sup> Marisela Vélez,<sup>‡,||</sup> José L. Carrascosa,<sup>§,||</sup> and Francisco Monroy<sup>\*,†</sup>

<sup>†</sup>Departamento de Química Física I, Universidad Complutense, 28040 Madrid, Spain

<sup>‡</sup>Instituto de Catálisis y Petroleoquímica, CSIC, Marie Curie 2, Cantoblanco, 28049 Madrid, Spain

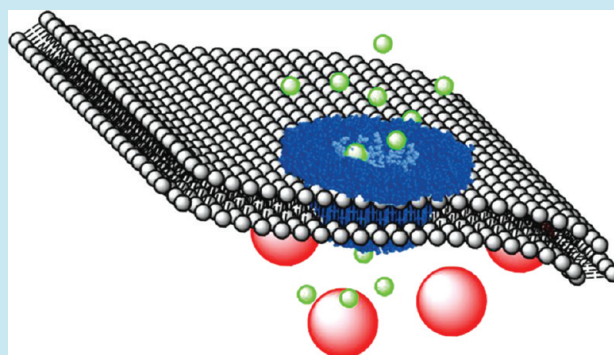
<sup>§</sup>Centro Nacional de Biotecnología, CSIC, c/Darwin 3, Cantoblanco, 28049 Madrid, Spain

<sup>||</sup>Instituto Madrileño de Estudios Avanzados en Nanociencia (IMDEA Nanociencia), Cantoblanco, 28049 Madrid, Spain

**ABSTRACT:** The portal connector of bacteriophage viruses constitutes a robust molecular machine for DNA translocation. In this paper we propose an optimized reconstitution method for efficient orthogonal integration of native viral connectors into lipid bilayers, particularly of giant unilamellar vesicles. Our nanoengineering plan considers the hydrophilic connector protein of the bacteriophage virus  $\phi$ 29 integrated into a specifically engineered bilayer made of “hydrophylyzed” lipids. From the precise knowledge of the connector structure, the membrane chemistry was designed by tuning reactivity in the bilayer using specific functional lipids. We show details on the reconstitution methods and experimental evidence about the integration of the portal protein in the engineered membrane.

The proposed route provides an efficient method for orthogonal integration of native viral connectors into lipid bilayers in conditions adequate for functional DNA translocation. This concept could be potentially exploited in advanced nanotechnological realizations, particularly for the integration of these powerful machines into giant lipid vesicles with the aim of building a cargo-device useful for gene delivery applications.

**KEYWORDS:** bacteriophage  $\phi$ 29, DNA translocation, membrane pore, giant vesicles, membrane reconstitution, lipid membranes



The translocation of nucleic acids through different biological compartments is a fundamental event in different aspects of the cellular life cycle, *e.g.*, mRNA transport from the nuclei to the cytoplasm, cellular communication, infection, *etc.* Many of these events rely on the existence of macromolecular pores that function as sophisticated nanomachineries. These machines have to overcome a number of basic problems for efficient translocation of extended nucleic acid polymers, mainly derived from the charged nature of the polynucleotide molecules, as well as from their high intrinsic rigidity.<sup>1,2</sup> An interesting example for double stranded DNA translocation is offered by the packaging of the genome in bacteriophages.<sup>2</sup> The assembly of double stranded DNA bacteriophages follows a series of steps that are common to most of these viruses.<sup>3–7</sup> A small number of viral proteins assemble first into a prohead that later incorporates the DNA. The packaging machinery is located at a unique vertex of the prohead (the portal) and comprises the head–tail connector and the terminases, which are involved not only in the selection of the DNA to be packaged but also in the ATP-driven DNA translocation.<sup>7,8</sup> The packaging complex, or portal, is formed by the assembly of connector and terminases defining a hollow channel with a diameter slightly larger than the one of dsDNA.

These portals have been studied in detail in a number of phages:  $\phi$ 29, T4, SPP1, T3/T7,  $\epsilon$ 15, and P22. The connector is a pore-like structure that appears not only in bacteriophages<sup>9–12</sup> but also in other viral systems such as Adeno and Herpes viruses.<sup>13,14</sup> Despite the absence of a clear sequence homology, the structural analysis reveals a common topology, displaying a truncated cone shape composed of a dodecameric assembly with three general domains: stalk, wing, and crown.<sup>8,10,11,13,15,16</sup>

During recent years, a large number of studies have focused on the use of biological and solid-state nanopores for diverse applications, from counting single molecules to genome sequence approaches.<sup>17</sup> The high specificity of the viral connector for DNA translocation, together with its well-known structure, makes it an attractive system to bridge material engineering and synthetic structural biology in the context of the use of DNA-nanopores in synthetic tools and devices. Furthermore, the synthetic approach offers unique possibilities for the analysis of the physical mechanisms involved in polymer translocation along pore-like structures.

**Received:** January 20, 2012

**Published:** February 24, 2012



With the final aim to build a synthetic cargo-device with an active translocation capability, we propose using the connector of bacteriophage  $\phi 29$  as a DNA-specific nanopore inserted in lipid bilayers. The idea is however not new. Recent studies by Guo *et al.* have focused efforts on the synthetic integration of modified  $\phi 29$ -connectors (hereinafter p10 protein) into lipid bilayers.<sup>18–22</sup> The first reconstitution of an hydrophobically modified p10 protein in lipid bilayers (giant vesicles and supported planar membranes) was achieved by these authors,<sup>18</sup> who reported evidence of orthogonal insertion susceptible to give rise to translocation capability.<sup>19–22</sup> That method consisted of protein incubation in the presence of lipid bilayers made of dioleyl-*sn*-glycero-phosphatidylcholine (DOPC),<sup>18</sup> a typical fluid bilayer former.

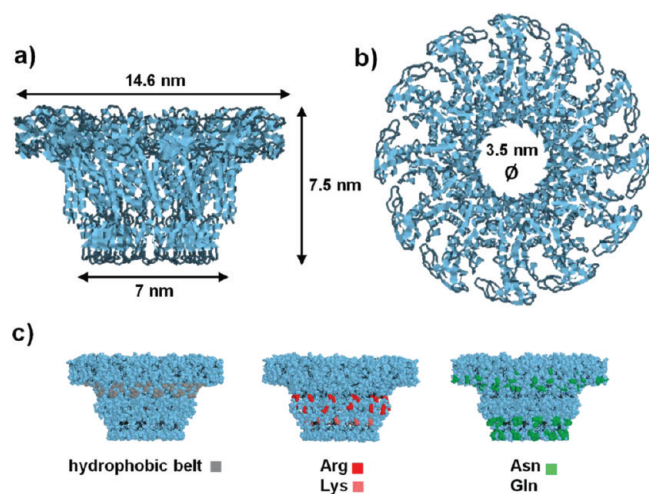
In this work, we propose an alternative synthetic route based on the chemical modification of the lipid bilayer for optimal insertion of the native p10 connector at orthogonal orientation. We propose a simple and robust synthetic concept based on the use of oxidized lipids able to chemically react with the outer surface of the connector protein. This strategy requires not only a detailed scanning of the connector structure for seeking functional groups adequate for lipid reactivity but also a proper structural matching at the hydrophobic core of the bilayer. Our engineering approach combines minimal protein manipulation with maximal membrane integration, resulting in an optimized number of portals orthogonally inserted in the membrane.

#### Surface Structure of the Native Connector (p10).

Figure 1 shows the 3D structure of the connector of phage  $\phi 29$ <sup>23</sup> as obtained from the PDB (PDB id: 1ijg). The atomic structure reveals that each of the 12 monomers of the connector protein that builds the connector has an elongated shape and is composed by a central, mainly  $\alpha$ -helical domain

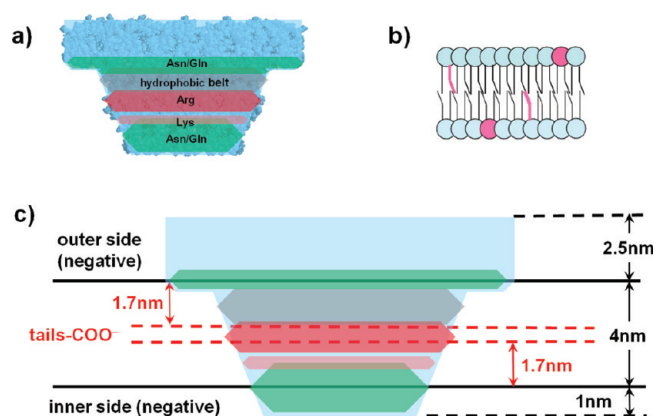
that includes a three-helix bundle, a distal  $\alpha$ - $\beta$  domain, and a proximal 6-fold stranded SH3-like domain.<sup>24</sup> The monomers assemble in a propeller-like dodecamer with an external diameter of 14.6 nm and a height of 7.5 nm (see Figure 1a). The dodecamer is a compact structure with a stalk and a wing structural domain, which also shows a conspicuous wide channel ( $\phi = 3.5$  nm diameter) that runs along the axis of the particle (see Figure 1b). The connector is oriented with the wing domain inserted in the viral shell, while the stalk extends outside the virus particle. The channel in the stalk region is built by a specific fold of  $\alpha$ - $\beta$  motifs that seems to be present in several connectors of different viral systems.<sup>8,10</sup> The surface of the internal channel has an overall electronegative character, and its entrance presents an acidic character (Glu189, Asp19, and Asp194).

Figure 1c shows chemical details of the external surface of the dodecameric particle p10. The complex presents a polar character in the wider wing domain, the area that is inserted into the interior of the viral head. Just below the wing domain, there is a belt of hydrophobic residues (Phe 24, Ile25, Leu28, Phe60, Phe128, Pro129, and Pro132; left panel in Figure 1c). It is noteworthy to mention that this 12-fold area of the connector is the one that contacts the five-fold vertex of the viral capsid, a symmetry mismatch that has been involved in different packaging model mechanisms. The stalk region has a surface with exposed charged residues (Arg17, Arg22, Lys172) at the equatorial location (Figure 1c; central panel), as well as several Asn and Gln residues concentrated at the two distal portions of the protein stalk (Figure 1c; right panel). All of these residues confer a whole hydrophilic character to the stalk area (Figure 1c). As surface-exposed basic residues could be potentially used for chemical bonding with carboxylic tailored lipids, we searched the surface reactivity of the p10 particle, focusing in the basic residues exposed to the surface exterior. Particularly, we found Arg17, Arg22, and Lys172, three surface exposed basic (positively charged) residues well suited for acid/base reactivity (red belts in Figure 1c). The guanidinium group of arginine (pK 13.6) was positively charged in acidic, neutral, and even most basic environments. Because of the conjugation between the double bond and the nitrogen lone pairs, the positive charge was delocalized, enabling the formation of stable intermediates by multiple hydrogen bonding responsible for the extreme basicity of guanidine against carboxylic acids. Consequently, exposed arginines of p10 might exhibit a strong reactivity against carboxylated lipids in moderately basic (pH 8) aqueous solution. Figure 2a shows the location of the reactive arginine residues exposed at the outer surface of the p10 complex. A dense distribution placed practically equatorial is present in the stalk portion, providing a highly basic reactive belt for optimal bonding with acidic lipid tails in the bilayer core. In addition, the lateral group in lysine is a primary amine behaving as a weaker base than arginine in aqueous solution (pK 10), consequently with a relevant, but significantly lower, reactivity against oxidized lipids. Therefore, in the present work we decided to use fluid lipid bilayers doped with a small amount of PAzPC (10% molar), an oxidized lipid with the short saturated chain (C0:9) tailored with a carboxylic acid group (see Figure 2b). At moderately basic pH ( $\approx 8$ ), the end group appeared predominantly deprotonated in the negative carboxylate form. Consequently, when included in a bilayer this charged tail might reverse the RCOO<sup>−</sup> group that became exposed at the aqueous outer surface. This reactive exposure might allow for adequate binding of lipids tails to primary



**Figure 1.** (a) Three-dimensional structure of the p10 connector ( $\phi 29$ -bacteriophage) as viewed from its lateral side. The circular dimensions correspond to the outer diameter of the crown (14.6 nm) and distal stalk (7 nm) portions. The object thickness is 7.5 nm, larger than a typical lipid bilayer (ca. 4 nm). (b) Plan top view of p10; dimensions: 14.6 nm outer diameter, 3.5 nm inner diameter of the central pore. (c) Axi-symmetric distribution of relevant aminoacids exposed to the outer surface of the p10 dodecamer (see text for details). Left panel: most hydrophobic exposed rests concentrate at the northern stalk just below the wing (gray). Central: basic rests (Arg/Lys) in the stalk portion at near equatorial emplacement (Arg: red; Lys: light red). Right: surface distribution of hydrophilic aminoacids with positive charge (Asn/Gln: two green belts).





**Figure 2.** Architectural description of the lipid-p10 protein membrane assembly. (a) Surface chemistry of p10 connector: highly hydrophobic belt for adhesive interaction with lipid tails (in gray); equatorial arginine and lysine residues with for reactive interaction with PAzPC (in red); distal cationic belts (Asn/Gln at pH 8) for electrostatic coupling with the negatively charged membrane surface (in green). (b) Lipid bilayer: The lipid component is based on DOPC (blue heads) mixed with the functional oxidized lipid PAzPC (10% mol; red tails) and the anionic lipid POPG (10% mol; red heads). (c) Protein-lipid membrane complex: the lipid bilayer is 4 nm thick, with the functional carboxylate groups ( $-\text{COO}^-$ ) of PAzPC dangling 1.7 nm below the membrane surface. The anionic lipid (POPG) endows net negative charge to both surfaces. The surface groups in the native p10 protein interact with the modified bilayer at different levels: (i) electrostatic counterbalance Asn/Gln-POPG at the membrane surface; (ii) hydrophobic matching at the near-surface hydrophobic core; (iii) Arg(Lys)-PAzPC amidation at the intermonolayer region.

amine rests in the p10 connector surface. When reactive amidation occurs the respective charges are counterbalanced, the resulting  $\text{RCOO-NH-p10}$  group being easily accommodated at the bilayer core with a reduced electrostatic penalty. The reversed tails of oxidized lipids provided covalent reactivity for surface exposed basic aminoacids in p10, mainly arginine and lysine.

At the moderately basic conditions considered here (pH 8), the amide aminoacids asparagine (Asn) and glutamine (Gln) are in the positive ammonium form. These rests were found also exposed at the outer surface of p10, principally as two positively charged belts located at distal locations with respect to the equatorial position (see green belts in Figures 1c/2a). The first Asn/Gln distribution is concentrated at the inner edge of the upper crown, 2.5 nm deep with respect to the major radius surface of the connector. The second one is a sparse distribution at the base of the stalk. As compared to basic amines (Arg, Lys), these amides are very weak bases and thus without reactivity interest at moderate basic pH. However, these two coronas endow excess positive charge adequate for optimal electrostatic association with negative lipid membranes. Thus, negatively charged lipids, with the phosphatidyl-glycerol head, for instance, should be included in an optimized formulation (see Figure 2b).

**Integration Strategy: Hydrophilizing the Membrane with Oxidized Lipids.** Because of their acid reactivity, oxidized phospholipids with hydrophobic tails barbed with a carboxylate moiety are known to bind membrane receptors and proteins.<sup>26,27</sup> Different proteins rich in amine lateral group basic amino acids have been shown to strongly bind to micellar aggregates of oxidized lipids.<sup>28</sup> The extent of binding is reduced upon lowering the pH, which would protonate the carboxylic

acid and thus reduce reactivity.<sup>29,30</sup> Furthermore, owing to their atypical structure (one shorter and polar acyl chain), these lipids are expected to alter the physical properties of the lipid bilayer membrane. Their organization properties were investigated Sabatini *et al.*<sup>31</sup> by measuring force area and surface potential isotherms in conjunction with fluorescence microscopy in mixed monolayers with DPPC. The results revealed an overall monolayer expansion due to the extended configuration of the oxidized chains into the aqueous phase. In bilayers, the authors suggested a reorientation of the hydrophilic tailed chain so avoiding the large energy penalty of embedding a charged group in the hydrophobic core. Further evidence for complete reversal of the oxidized acyl chain was recently confirmed by Mouritsen *et al.*<sup>28</sup> from MD simulations.<sup>28</sup> The presence of chain-reversing charged lipids might directly affect bilayer structure of typical phospholipids. Particularly, the chain order and packing profiles are both expected to reduce, thus resulting in a significant softening.<sup>28</sup> Regarding electrostatic effects, the presence of net negative charge in oxidized lipids was found to effectively lower the phosphate-choline dipole near the interface.<sup>28</sup> Therefore, the acidic tails are expected not only to react with the basic groups of the p10 protein but also to disrupt the lipid packing causing a structural plasticity playing in favor of connector insertion.

With the objective to spatially modulate lipid-protein interactions at different levels in the bilayer, we have taken advantage of the surface chemistry of the connector protein, which is distributed as parallel belts formed by 12-fold axial repetitions of exposed residues with different chemical affinities. In Figure 2a, the four relevant parallel surface regions in the stalk portion are shown: the reactive (pH 8) Arg/Lys equatorial belt (left), the northern one formed by hydrophobic aminoacids (center), and the southern one constituted by cationic Asn/Gln residues (right). Figure 2b is a schematic of the lipid bilayer, based on DOPC supplemented with 10% of reactive lipid PAzPC tailored with an acid chain and 10% of anionic-head DOPG. The cartoon in Figure 2c depicts the structural scenario for orthogonal insertion, where the p10 connector interacts at these three different levels with the lipid bilayer. As structural bilayer former, we considered DOPC (C18:1), a fully unsaturated phospholipid combining packing ability typical of phosphocholine head with chain disorder sufficient to form stable bilayers with low rigidity and high fluidity.<sup>32</sup> The two unsaturated chains endowed conformational plasticity and thus an enhanced capacity to match the thickness of different embedded objects.<sup>33</sup> The average thickness of single DOPC bilayers is 4.0 nm (Figure 2c), as determined by X-ray scattering<sup>34</sup> and AFM,<sup>35,36</sup> a size 3.5 nm thinner than the transverse height dimensions of the p10 complex (Figure 1a). The considered oxidized lipid (PAzPC) had the same phosphocholine head as DOPC linked to a palmitoyl saturated chain (C16:0) nearly matching the thickness of the DOPC matrix. The COOH-tailored chain was C8:0, a length half the thickness of the palmitoyl core (C16:0). This determines the position of the reactive carboxylate group (lipid- $\text{COO}^-$ ) at a distance 1.7 nm beneath the outer bilayer surface (Figure 2c). This acid group could efficiently react with the basic Arg/Lys-belt of p10. Consequently, when stabilized inside the hydrophobic core of the bilayer as a non-charged amide ( $-\text{COO-NH-p10}$ ), the resulting covalent linkers will nearly accommodate the equatorial belt of p10 as a non-charged element in the central, intermonolayer region of the lipid bilayer (see Figure 2c; red dashed bands).

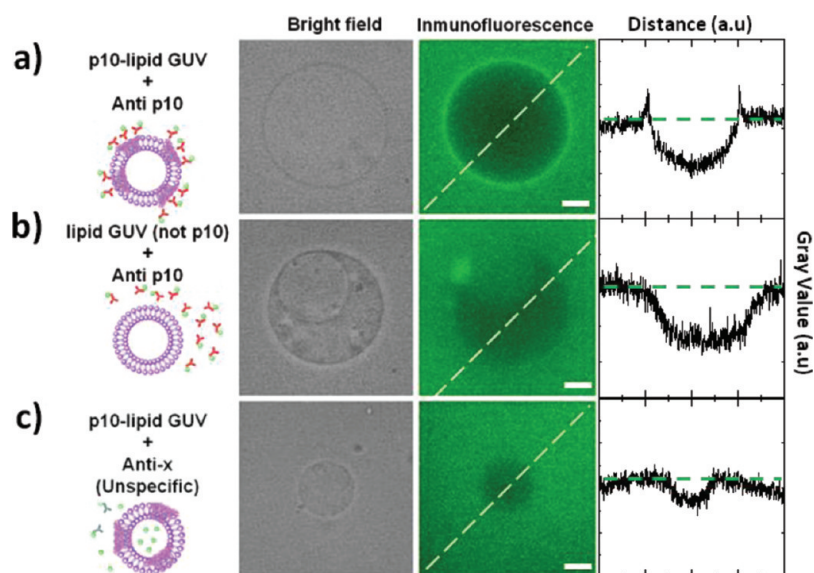


**Figure 3.** Immunofluorescence tests on giant vesicles based on the reactive lipid component (DOPC + 10% PAzPC + 10% POPG). The fluorescence intensity profiles in the right panels evidence either the presence (positive) or depletion (negative) of fluorescent antibody with respect to the average concentration in the incubation medium (dashed line). (a) Positive: GUVs prepared in the presence of p10-protein show an increased concentration of the specific fluorescent antibody in the membrane site, thus indicating p10 integration. (b) Negative control: GUVs prepared in the absence of p10-protein are not fluorescently labeled by the specific anti-p10 antibody. No higher fluorescence intensity is detected in the membrane site, the intensity profile varying monotonically to a negative value, corresponding to dye depletion, in the vesicle lumen. (c) Blank control: an unspecific fluorescent antibody fan does not label the vesicles prepared in the presence of p10-protein.

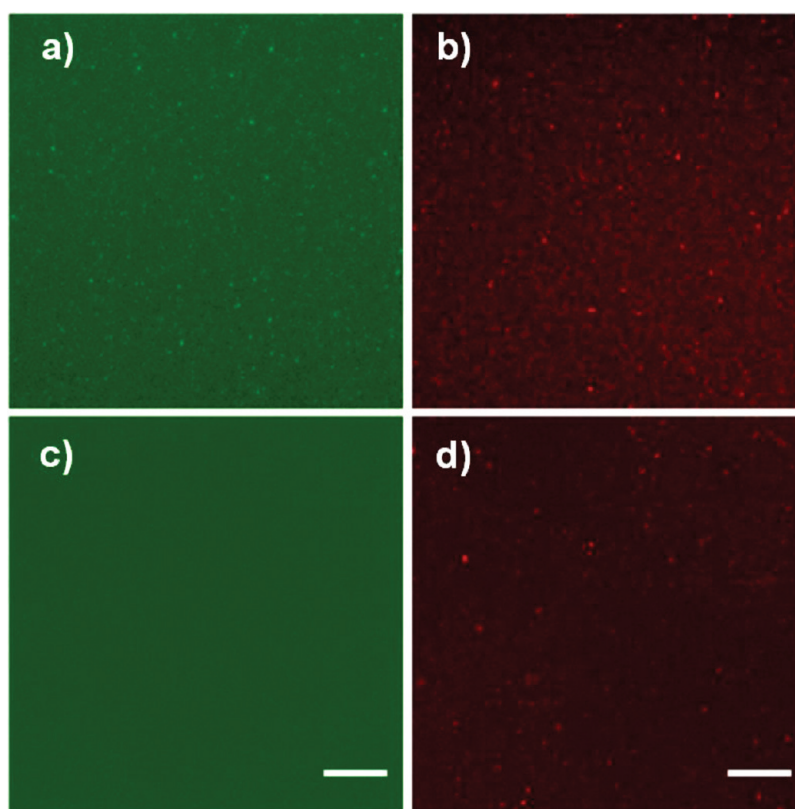


**Figure 4.** Permeability experiments where the retention of fluorescent probes of different size is tested by confocal microscopy in LUVs. The probes used were calcein, a low molecular weight probe diffusible across p10 pores (green channel; a, c), and rhodamine-dextrane (rhDx), a large polymeric probe not able to trespass the tight p10 pores (red channel; b, d). Top panels: full-retention control. The vesicles were prepared in the absence of protein, thus both probes, calcein (a) and rhodamine (b), are retained inside. Bottom panel: size-selective retention. When prepared in the presence of p10 protein, porous vesicles show selective permeability to small objects (calcein; c) and retention against large polymer molecules (rhDx; d).

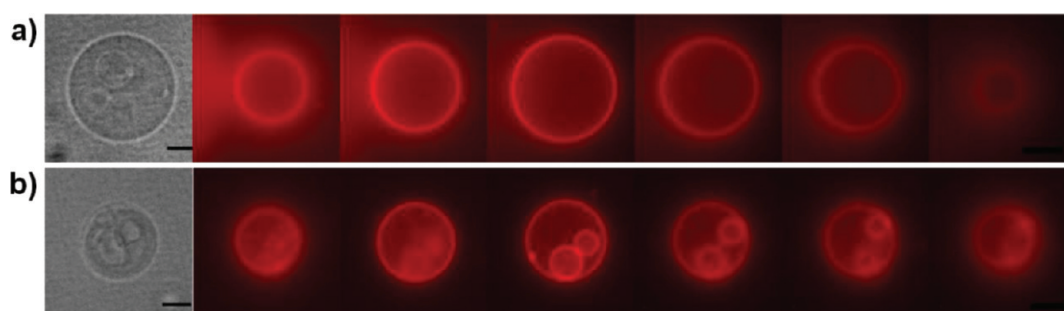


**Figure 5.** Permeability experiments in oligolamellar vesicles. Access to the internal compartments of the soluble dye FM1-43 (added from the outer solution) evidence membrane porosity and connectivity with internal compartments through p10 connector. Oligolamellar GUVs prepared (a) in the absence (control) and (b) in the presence of protein (positive).

Furthermore, the negatively charged phospholipid DOPG was included to endow the bilayer with a negative surface charge (Figure 2b) adequate for electrostatic matching with the two distal positive belts of p10, mainly constituted by Asn and Gln (see Figure 2a/c; green bands).

Finally, if orthogonal integration occurs, additional hydrophobic matching between the acyl lipid chains and the hydrophobic belt of p10 is expected at the outer core of the lipid bilayer (see Figure 2a/c; gray band).

## RESULTS AND DISCUSSION

**Membrane Integration in GUVs: Immunofluorescence Detection.** Figure 3 shows immunofluorescence evidence for protein integration in the lipid bilayer of giant unilamellar vesicles electro-swelled in the presence of p10-connector (see Methods). When p10 was present (Figure 3a), the p10-specific dye antibody revealed p10 accumulation in the membrane with respect to the bulk solution (see intensity profile in Figure 3; top panel), a clear evidence for protein integration in the membrane. Consistently, no enhanced membrane fluorescence is observed in the absence of connector or when an unspecific antibody was used in the presence of p10-GUVs, the dye being found homogeneously distributed in the solution (Figure 3b,c). In the later case, the unspecific antibody was indeed observed in the solution but did not accumulate in the membrane. From these results, the membrane integration of the p10 connector was unambiguously determined; however, nothing was known about its orientation with respect to the bilayer plane.

**Permeability Tests.** Orthogonal integration with respect to the bilayer plane is a first requirement for functional translocation of DNA by the portal protein. To obtain evidence for a possible orthogonal orientation, we performed three different tests where the permeability of different fluorophores across the pores was checked by fluorescence microscopy.

**Size-Probe Retention in LUVs.** The lipid bilayer is known to be a permeability barrier against hydrophilic molecules.<sup>39</sup> Calcein is a water-soluble low molecular weight fluorescent dye ( $M_w = 622.53$  Da), well-known to be efficiently retained inside liposomes.<sup>40</sup> However, calcein is sufficiently small to permeate across the 3 nm diameter p10 pores. On the other hand, rhodamine-labeled dextran (rh-Dx;  $M_w = 70$  kDa,  $R_g \approx 20$  nm) is a polymer dye that should be unable to go through the p10 pore ( $R_g \approx 20$  nm  $\gg \phi = 3.5$  nm). Relatively large proteoliposomes (1  $\mu$ m diameter) were prepared by co-extruding lipid suspension with the protein solution (see LUVs for Confocal Microscopy in Methods). The proteo-LUVs were prepared in the presence of rhodamine (0.5 mM; Figure 4a) and calcein (0.5 mM; Figure 4b), and then the vesicle

suspensions were observed under a confocal microscope (see Methods). Figure 4 shows the confocal fields imaged 24 h after dilution. Let us first discuss the control case in the absence of protein. In Figure 4a,b (top panels), the presence of fluorescent spots suspended in a darker background clearly reveals fluorophore retention inside liposomes, independently of the probe size. Similar images are obtained at longer times, confirming the barrier character of the lipid bilayer for both dyes (calcein, Figure 4a and rhodamine-dextran, Figure 4b). Then, p10-proteoliposomes were prepared by co-extrusion of the lipid suspension (16 mg/mL lipids, 0.5 mM calcein, 50 mM Tris-HCl, pH 7.8, 200 mM NaCl) in the presence of protein at a very low content with respect to lipids (1/200,000 P/L molar ratio). Similarly to the control test, the proteoliposome suspension was diluted in dye-free buffer (1:4 v/v). Figure 4c,d (bottom panels) show images taken in the presence of protein. The fluorescence of the small fluorophore calcein eventually becomes equilibrated in and outside the vesicles, indicating that the presence of p10 portal proteins endows porosity to the membrane. The high-molecular-weight dye rhodamine-dextran however does not permeate through the small pores and remains efficiently entrapped inside the vesicles. Therefore, vesicles are not visible in the green channel corresponding to calcein (Figure 4c) but are clearly discernible in the red channel corresponding to rhodamine-dextran (Figure 4d).

**Pore Connection to Internal Compartments.** To confirm the presence of orthogonally oriented pores we have taken advantage of the fluorescent emission of FM1-43, an extrinsic water-soluble probe having high quantum yield in hydrophobic environments that becomes completely quenched in aqueous media.<sup>41</sup> In addition, this dye exhibits high affinity for lipid environments but is impermeable to membranes. In a vesicle suspension, because water molecules strongly quench FM1-43 fluorescence, emission is observed only once incorporated into the lipid bilayer. Consequently, when added in the outer suspending medium the dye might label only the external leaflet of lipid vesicles. However, if water pores were present in the membrane, the probe should be able to cross inside the vesicle lumen, gaining access to internal compartments (eventually, internal membranes in oligolamellar vesicles). We prepared giant vesicles with an oligo-lamellar structure and checked the dye action of FM1-43 to test its transport in the absence or in the presence of pore channels allowing communication between internal compartments. Figure 5 shows a typical FM1-43 permeability test. The oligolamellar character was revealed in the bright field images. The fluorescence images show a tomographic scan of the same vesicle between their two



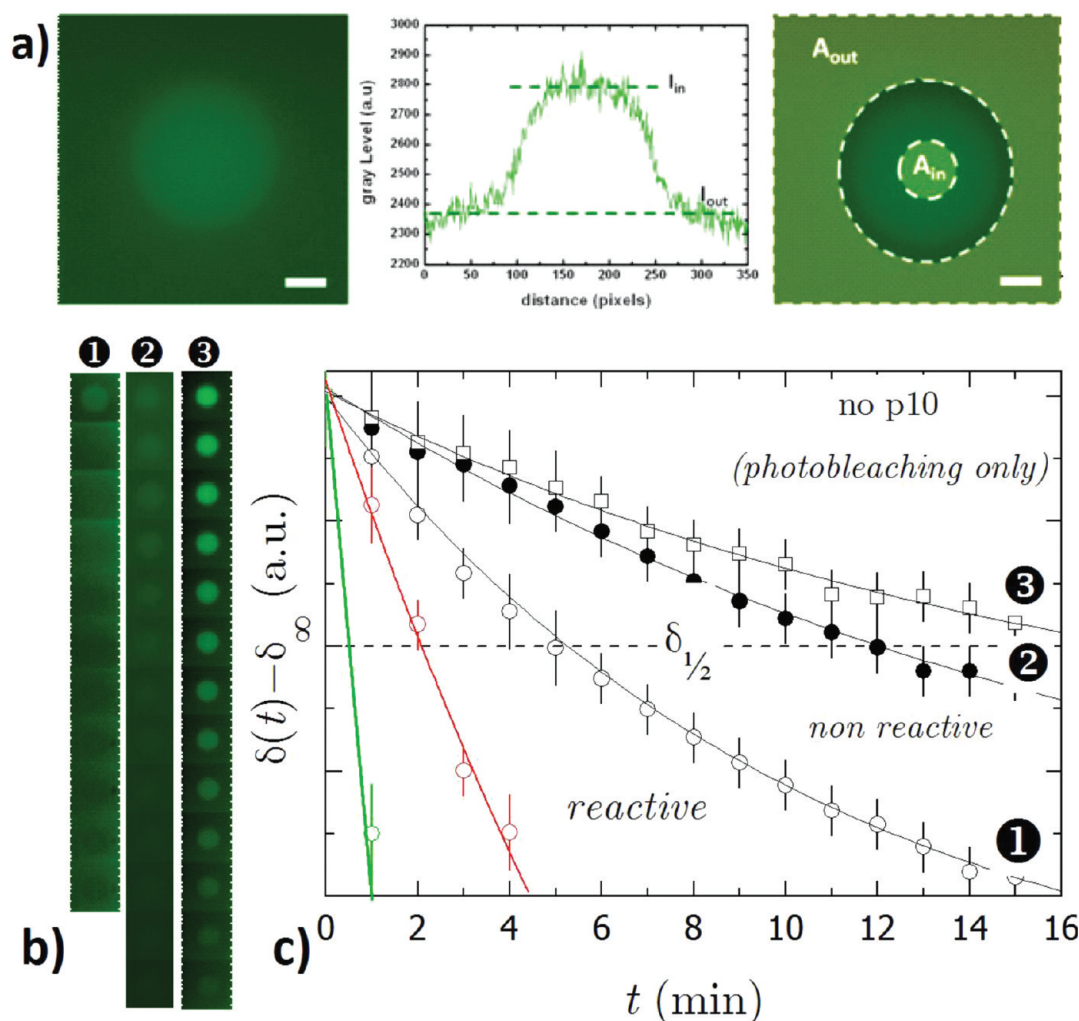


**Figure 6.** Calcein-permeability kinetics. (a) Image analysis. A given vesicle filled with calcein (left panel) is digitized in ImageJ as a spherical distribution with inner fluorescence intensity  $I_{in}$  higher than the external background  $I_{out}$  due to residual calcein after washing out (central panel). For quantitative calculation of the normalized intensity  $\delta(t)$  using eq 1, we used the integrated area of the external background  $A_{out}$  with average intensity  $I_{out}$  and the integrated area of the inner core  $A_{in}$  where the maximal intensity  $I_{in}$  is recorded. (b) Kinetic recording of a typical GUV prepared: ① with p10-portals integrated in a reactive DOPC-bilayer containing PAzPC (10%) and DOPG (10%); ② with p10-portals incubated with a non-reactive DOPC-bilayer, and ③ without protein. (c) Normalized intensity decays corresponding to different kinetic experiments as in panel b: ① p10 integrated in the reactive bilayer (open circles); ② p10 integrated in the non-reactive bilayer (●); ③ no protein, DOPC only (□). Three different protein concentrations were checked in the reactive-integration schema: P/L = 1/370,000 (black ○); 1/37,000 (red ○); 1/3,700 (green ○). The experimental curves are shifted with the infinity intensity  $\delta_{\infty}$  recorded at a very long time, typically 1 h after beginning the experiment. The dashed horizontal line represents the half-life level for estimating the characteristic decay time,  $\delta(t) = \delta_{1/2} = 1/2$  at  $t = \tau_{1/2}$ . Continuous lines are a simple visual guide. The experimental values correspond to an average over a population of 20 different vesicles recorded in different experiments. The error bars correspond to standard deviations.

poles (the central image typically corresponds to the equatorial plane). When no protein is present (Figure 5a), the fluorescent probe remained at the outer leaflet of the external membrane, the internal compartments remaining inaccessible to the fluorescent dye (no fluorescent emission is detected in this case from the internal membranes). However, in the presence of portal protein (Figure 5b), the existence of different internal compartments was clearly revealed in the fluorescence images, a fact possible only if probe transport across the membranes is assumed. Consequently, the data confirmed the presence of open portals orthogonally integrated in the membranes, thus allowing for connecting different compartments to permeating water and solutes.

**Permeability Kinetics in GUVs.** From the above experiments, we deduced the existence of membrane integration of the

connector portal at orthogonal orientation. Oxidized lipids were used as a covalent linker favoring membrane incorporation through covalent anchoring at the hydrophobic core of the bilayer. Consequently, a larger integration yield is expected from the present reactive strategy than under simple incubation with an inert bilayer. To verify this point, we comparatively probed permeation kinetics in single GUVs prepared (a) in the presence of oxidized lipids (10% PAzPC molar content) at a relatively low protein to lipid molar ratio (P/L = 1/70,000) and (b) in the absence of oxidized lipids at comparatively much higher protein content (P/L = 1/75). Fluorescence-loss experiments were probed by optical microscopy in single GUVs containing different dyes. As above, we used calcein, a small green probe able to permeate through narrow channels, and rhodamine-barbed dextran (70 kDa), the negative

permeability control unable to transpose through connector pore. In these experiments, GUVs and proteoGUVs were prepared in the presence of equal amounts of the two fluorescent probes (dye 1 mM; buffer: sucrose 200 mM, TrisHCl 50 mM, NaCl 200 mM) following the standard procedure described in Methods. Prior to observation by microscope, the suspension was centrifuged in an Eppendorf tube (45,000 rpm, 1 h). Then, a small aliquot (10  $\mu$ L) was carefully pipetted from the vesicle sediment and dissolved in a drop of buffer solution (containing no fluorescent probes; buffer: 208 mM glucose, TrisHCl 50 mM, NaCl 200 mM) previously placed on a microscopy slide. This protocol allowed for accurate time-recording of fluorescence 1 min after mixing, the time necessary for vesicles to sediment and become visible in the microscopy field. No significant dye release is expected during such a short lag time. Depending on the number of pores, this delay effect produced an undetermined initial decay in the fluorescence signal, preventing an absolute comparison between different vesicles. However, the fluorescence intensity decays can be normalized relative to the initial intensity measured at an arbitrary initial time ( $t_0 = 1$  min) and compared between vesicles. Probe photobleaching was minimized by recording discrete fluorescence images every minute at a short exposure time (100 ms). Accidental photobleaching was prevented by localizing a given GUV in bright field and then recording its fluorescence intensity in the corresponding fluorescence channel. The following vesicle analyzed was chosen far away from the former observation field, eliminating previous exposure to the excitation beam. Figure 6 shows kinetics recorded in the calcein channel. From a quantitative standpoint, fluorescence losses can be quantified as the difference in averaged intensity between the vesicle lumen and the bulk exterior (see schematic in Figure 6a):

$$\delta(t) = \frac{A_{\text{in}}I_{\text{in}}(t) - A_{\text{out}}I_{\text{out}}(t)}{A_{\text{in}} + A_{\text{out}}} \quad (1)$$

where  $I_{\text{in}}$  and  $I_{\text{out}}$  represent the integrated intensities in the inner circle and in the outer sector, respectively. The intensities are weighted by the respective areas  $A_{\text{in}}$  and  $A_{\text{out}}$ . The images were treated using ImageJ (<http://imagej.nih.gov/ij/>).<sup>42</sup> For every case, about 15–20 vesicles were analyzed, the final relative intensities being a statistical average performed over a vesicle population.

Panel ① in Figure 6b shows a typical vesicle where p10 portals were membrane-inserted following our reactive strategy at P/L = 1/70,000 protein-to-lipid molar ratio. The initial fluorescence level was in this case relatively weak, suggesting significant probe losses during the initial lag time. In the next two frames (2 min after  $t_0$ ), the fluorescence intensity between the lumen and vesicle exterior was practically equal, suggesting a rapid diffusion of calcein across the portal pores. At longer times ( $t > 2$  min), the content loss was so efficient that calcein was observed more brilliant in the surrounding medium than in the vesicle lumen, the relative intensity becoming negative at enough long times ( $\delta_{\infty} < 0$ ). This is a fact closely related to the facilitated free diffusion of the fluorescent probe from a practically infinite bulk reservoir with respect to the relatively impeded diffusion through the pores, i.e., once diffused out from the vesicle interior, calcein is replaced faster in the accessible outer volume than in the restrained inner lumen. For comparison, a similar time recording for vesicles with connectors inserted in non-reactive conditions (DOPC

membrane; no PAzPC, no DOPG, pH 7) is shown in panel ② of Figure 6b. Similarly to the former case, a weak contrast was observed at starting time ( $t_0$ ), suggesting calcein loss through the pores during the incubation lag time. However, the relative loss of fluorescence from the vesicle lumen was observed to be comparatively slower in this case than in the former one, a fact intrinsically related to the existence of a smaller number of transporting pores in the non-reactive case. Spurious fluorescence losses due to intrinsic photobleaching were probed in control experiments performed in the total absence of p10 protein (Figure 6b; panel ③). As expected for a total retention case, the initial calcein intensity was found to be high inside the vesicles. Very slow intensity decay was observed with time, a clear sign of probe trapping inside the vesicle (the fluorescence decay being representative of probe photobleaching).

The numerical results are plot in Figure 6c, which collects the averaged kinetic curves calculated with eq 1 for the three cases in Figure 6b. A fast decrease of fluorescence contrast is observed for vesicles with p10 portals integrated by the covalent strategy using oxidized lipids. A correlated behavior was observed at different P/L ratios: the higher the protein content the faster the fluorescence decay (see Figure 6; open circles). This demonstrates the quantitative correlation between the amount of integrated protein and the strength of pore functionality achieved in the reactive schema. For these vesicles at reactive conditions, the fluorescence loss is characterized by a very short decay time, e.g., at P/L = 1/37,000, the decay time was found as short as  $\tau_{\text{react}} \approx 2$  min (defined as an average half-life time when  $\delta(t = \tau_{1/2}) = 1/2$ ). However, for vesicles prepared with the same protein content (P/L = 1/37,000) at non-reactive conditions, the characteristic emptying time was found considerably longer,  $\tau_{\text{nonreact}} \approx 12$  min (see Figure 6c; case ②), indicating a slower calcein loss through a reduced number of membrane pores, significantly smaller than in the reactive method using oxidized lipids. Indeed, the decay in fluorescence intensity was found in that case similar to the intrinsic calcein photobleaching measured when no protein is present (Figure 6c; case ③). In this control, vesicles were prepared in the absence of protein with the same lipid cocktail as in the reactive case (DOPC/PAzPC/DOPG), thus assuring an adequate comparison with the permeability experiment. Assuming that the rate for calcein diffusion across the membrane is proportional to the number of translocation portals, the relative amount of membrane pores can be estimated as  $\rho_{\text{react}}/\rho_{\text{nonreact}} \approx \tau_{\text{nonreact}}/\tau_{\text{react}} \approx 6$ . However, the decay curve was found practically equal in the non-reactive case (②) as for the photobleaching curve (③), suggesting a low dye permeability caused by a small fraction of open portals integrated at orthogonal configuration. Consequently, the integration yield by the covalent strategy using oxidized lipids (case ①) is at least 6-fold higher than by the simple incubation method (case ②).<sup>18</sup>

As a control for blocked diffusion across p10-pores, we show in Figure 7a results for the fluorescence intensity decay of the high- $M_w$  dye (rhodamine-dextran) in the same three cases as with calcein. Because such a polymer coil is unable to traverse the p10 channel, vesicles containing membrane pores exhibit a fluorescence decay similar to the photobleaching control. Consistent with our prediction, kinetic data in Figure 7b show similar behavior, thus confirming the retention of the large molecules inside the vesicle lumen independently of the membrane components.



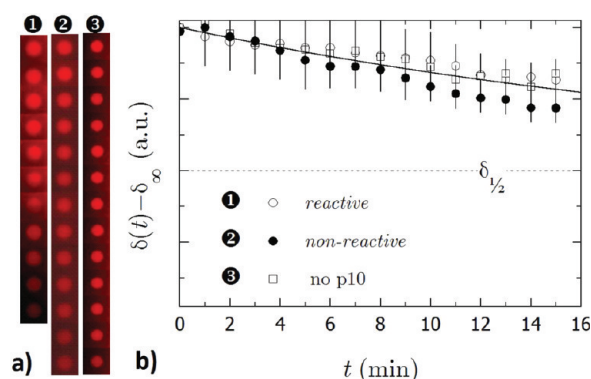


**Figure 7.** Rhodamine-dextran permeability kinetics. (a) Kinetic recording of a typical GUV prepared: ① with p10-portals integrated in a reactive DOPC-bilayer containing PAzPC (10%) and DOPG (10%); ② with p10-portals incubated with a non-reactive DOPC-bilayer, and ③ without protein. (b) Normalized intensity decays corresponding to different kinetic experiments as in panel a: ① p10 integrated in the reactive bilayer (○); ② p10 integrated in the non-reactive bilayer (●); ③ no protein, DOPC only (□). As in Figure 6, the curves are shifted with the infinity intensity  $\delta_\infty$ . The experimental values correspond to an average over population of 20 different vesicles recorded in different experiments. The error bars correspond to standard deviations.

**Structural Analysis by AFM.** Atomic force microscopy was used to explore the incorporation of the connectors into the bilayer. Liposomes containing the protein were incubated over a mica surface in the presence of (50 mM TrisHCl, 150 mM NaCl, 10 mM MgCl<sub>2</sub>, and 10 mM CaCl<sub>2</sub>), conditions under

which lipid vesicles fuse forming planar lipid bilayers. AFM images of the lipid surfaces were taken operating the microscope in the jump mode.<sup>43</sup> Figure 8A shows the lipid surface formed from liposomes of the same lipid composition but without protein inserted. The presence of oxidized lipids in the mixture allowed the formation of smooth membranes of *ca.* 4 nm thickness (Figure 8A; bottom panel), a value compatible with the accepted thickness of supported lipid bilayers. Vesicles with incorporated connector over a large range of protein–lipid molar ratio (P:L = 1/37,000 to 1/1,000) were also able to fuse on the mica surface. A typical AFM image (P/L = 1/37,000) is shown in Figure 8B1. Here, we can discern inserted connectors ( $\alpha$ -configuration) from brighter grains corresponding to thicker objects sitting on the membrane. The thickness of these larger objects is *ca.* 7 nm (Figure 8B1; left panel), a size compatible with the dimensions of single connector units not integrated in the membrane ( $\beta$ -configuration; see cartoon in Figure 8B1). Figure 8B2 shows a high-resolution zoom of the square area delimited in Figure 8B1. Inside this membrane sector we count a number  $n_p = 28$  of single protein objects integrated in the bilayer (Figure 8B2;  $S = 1 \mu\text{m}^2$ ). The surface density of integrated protein can be estimated with respect to lipids as  $n_p/n_l$ . Here,  $n_l$  is the number of lipid molecules inside the considered membrane sector,  $n_l = (S - n_p a_p)/a_l$ , which is mainly determined by the molecular area of the lipid molecule  $a_l \approx 0.8 \text{ nm}^2$ .<sup>44</sup> The lipid density is corrected by a factor  $-n_p a_p$ , the surface area occupied by protein molecules (a single protein occupies  $a_p = \pi R^2 \approx 167 \text{ nm}^2$ ;  $R \approx 7.3 \text{ nm}$ ). Consequently, for the membrane patch displayed in Figure 8B2, the relative density of integrated protein is estimated as  $n_p/n_l = n_p a_l / (S -$

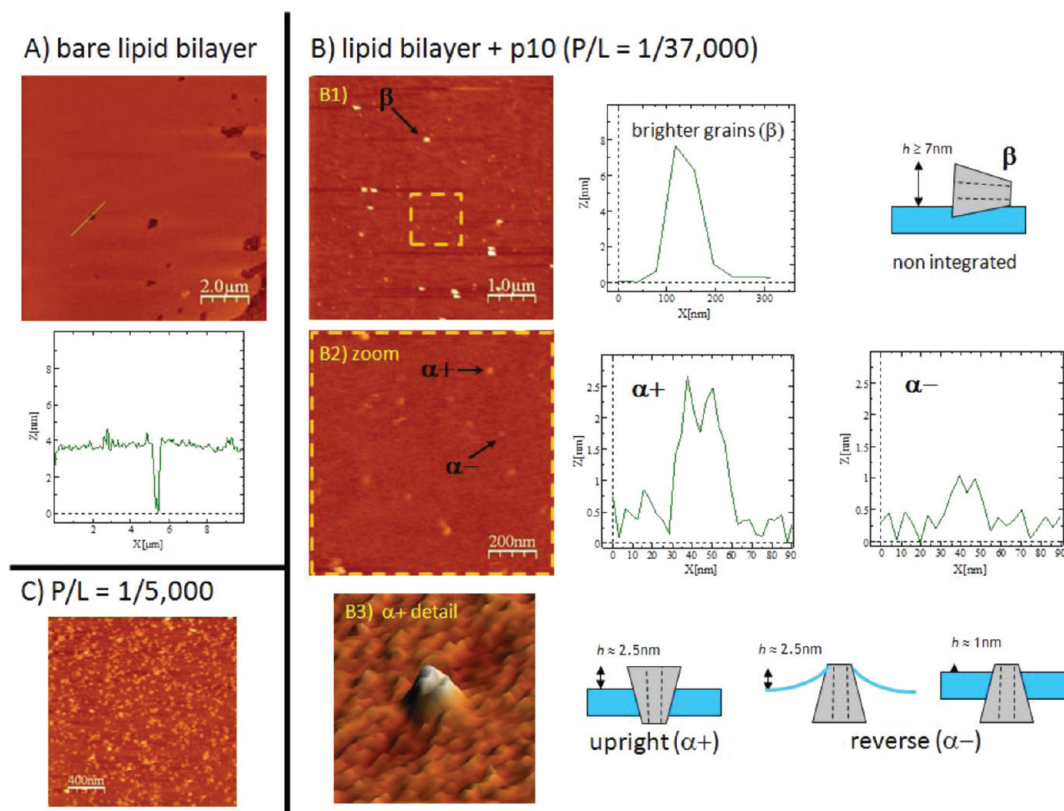


**Figure 8.** AFM structural analysis of native p10-protein integrated in a reactive bilayer (DOPC/PAzPC/DOPG; 8/1/1; pH 7.8). (A) Bare lipid bilayer. (B) Reactive bilayer incubated in the presence of p10-protein (P/L = 1/37,000). (C) Membrane integration at a higher protein content (P/L = 1/5,000).

$n_p a_p \approx 2 \times 10^{-5}$ , a value slightly lower but in rough quantitative agreement with the nominal P/L content of the proteoliposome preparation ( $P/L = 1/37,000 = 2.7 \times 10^{-5}$ ). This estimation confirms the proposed reactive schema with a high integration efficiency. A detailed analysis revealed the existence of two classes of membrane protrusions with different height and diameter. Particularly, the larger spots ( $\alpha+$ ) were found overhanging *ca.* 2.5 nm out with respect to the basal plane of the bilayer (Figure 8B2; right panel;  $\alpha+$ ), a size compatible with the dimensions of the crown portion of the connector (see Figure 1a and cartoon in Figure 8B2). Figure 8B3 enlarges one of these  $\alpha+$  grains at ultrahigh resolution. The presence of a central concavity in these objects confirms them as a portal element with an open pore. Among the 28 single proteins counted in Figure 8B2, we assign 17 to the thicker  $\alpha+$  objects (60%). Arguably, the connectors integrated in the reversed configuration ( $\alpha-$ ) might appear in the AFM images thinner and smaller than these orientated upright. However, because the flexible bilayer is topologically adaptive around the rigid connector (see cartoon in Figure 8; intermediate between  $\alpha+/\alpha-$ ), some of the larger spots could expectedly correspond to connectors in the reverse configuration. This could explain why one counts an apparently fewer proportion of smaller objects with the reversed configuration (in Figure 8B2; 11  $\alpha-/28$  total, 40%). The smaller objects found in the AFM images were observed significantly thinner (*ca.* 1 nm; see Figure 8B3; right panel), a qualitative set of dimensions compatible with the  $\alpha-$  reversed configuration of the connector. In this case, the observed object could correspond to the distal portion of the connector stalk protruding out the bilayer plane. Therefore, although the results suggest a mutual equivalence between the two different orthogonal orientations, *i.e.*,  $[\alpha+] \approx [\alpha-]$ , no unequivocal discrimination (nor of intermediate inclinations) is possible from the present experiments. Figure 8c shows a typical AFM image obtained at a higher protein concentration ( $P/L = 5,000$ ). Particle counting analysis with WSXM<sup>38</sup> provided a value  $n_p \approx 10^3$  of hill-like objects (with a height between 0.5 and 3 nm) found in the scanned area ( $S = 4 \mu\text{m}^2$ ). The estimated protein density was estimated to be  $n_p/n_l \approx 2 \times 10^{-4}$ , in close quantitative agreement with the nominal value,  $P/L = 2 \times 10^{-4}$ . Again, we confirm the membrane reactive schema with a high integration efficiency, even higher with increasing the protein content.

**Conclusions.** Efficient membrane integration of native p10-portals was pursued at orthogonal configuration. We have proposed a chemical route based on the spatial matching of the protein–lipid interactions at different levels in the lipid bilayer. Covalent, electrostatic, and hydrophobic cohesive interactions were promoted by introducing different functional lipids in the membrane formula. The protein was integrated in the functional lipid bilayer of giant unilamellar vesicles prepared at reactive conditions provided by moderately basic pH (7.8). With the objective of testing pore integration at orthogonal configuration, we performed permeability tests with different fluorescent probes. The unequivocal existence of material diffusion through the membrane pores was deduced from those studies. The kinetic analysis of the permeability data allowed for a quantitative estimation of the orthogonal integration rate at different experimental conditions. The orthogonal orientation was microscopically revealed from a detailed structural analysis performed by AFM. As a major conclusion, from a synthetic standpoint, the present reactive method is very efficient, orthogonal integration occurring at a quantitative extent

compatible with preparative P/L ratio. This integration efficiency is much higher than that reported by simple protein incubation at non-reactive conditions. Therefore, the new methodology proposed here offers a valuable route for the synthetic reconstitution of native connector proteins in lipid bilayers, particularly in the membrane of giant unilamellar vesicles. The method is particularly convenient for efficient orthogonal integration of viral connectors as DNA portals in lipid vesicles and potentially transferable as a robust synthetic protocol adequate for the fabrication of highly specific DNA-pores in advanced nanotechnological applications.

## METHODS

**Chemicals.** 1,2-Dioleoyl-*sn*-glycero-3-phosphocholine (DOPC), 1-palmitoyl-2-azelaoyl-*sn*-glycero-3-phosphocholine (PAzPC), and 1,2-dioleoyl-*sn*-glycero-3-phosphoglycerol (DOPG) were from Avanti Polar Lipids (Alabaster, AL). The dyes calcein and rhodamine-labeled dextran (40 kDa) were from Sigma, and FM1-43 was from Invitrogen. Solvents and other analytical grade chemicals were from Sigma. Deionized water was used from a Milli-Q source (resistivity higher than 18 M $\Omega$ /cm; organic content <2 ppb).

**Connector Production.** The connector complex was obtained from the protein p10 of *Bacillus subtilis* bacteriophage  $\phi$ 29. The gene coding for p10 was cloned in a recombinant plasmid pRSET-p10, which was overexpressed in *E. coli*. Protein p10 was purified by a two-step ion exchange chromatography, following the procedures described previously.<sup>25</sup> Protein p10 purified according to this protocol was found assembled as a dodecameric complex.<sup>24</sup>

**Buffer.** All of the lipid/protein preparations were suspended/dissolved in saline buffer compatible with the p10-assembled configuration (50 mM TrisHCl, pH 7.8, 200 mM NaCl).

**Large Unilamellar Vesicles.** Large unilamellar liposomes (LUVs) were prepared by the extrusion method from mixtures of the three different lipids (DOPC, DOPG and PAzPC) in molar ratio 80:10:10. Lipids were dissolved in chloroform/methanol solution (1/1 v/v). This solution was later dried under a nitrogen stream forming a lipid film. Then, the film was hydrated by vortexing and further resuspension in buffer at 1 mg/mL total lipid concentration. The resulting multilamellar suspension was extruded through a polycarbonate membrane with 1  $\mu\text{m}$  nominal pore diameter (Avestin, Germany). After 21 extrusion cycles, large unilamellar vesicles (LUVs) were obtained at high concentration and relatively low size polydispersity (as verified by DLS; data not shown). For protein incorporation, p10-lipid proteo-LUVs are formed by co-extrusion of the lamellar suspension with the protein solution. The protein was added during the hydration step before extrusion. Finally, LUVs (or proteo-LUVs) are concentrated at 10 mg/mL (45,000 rpm; 4  $^{\circ}\text{C}$ , 1 h).

**Giant Unilamellar Vesicles (GUVs).** These were prepared by the electrosweeling method from LUVs of the three different lipids (DOPC, DOPG and PAzPC; molar ratio 80:10:10). Briefly, 10  $\mu\text{L}$  of LUV buffer dispersion (10 mg/mL total lipid) was spread in an ITO (indium tin oxide)-coated glass slide. The fabrication chamber is composed of two parallel slides separated by a Teflon spacer (1 mm thickness). After solvent evaporation, the film was rehydrated with a sucrose solution (300 mM). The chamber was then connected to an AC power supply (1.1 V, 8 Hz; 90 min). Calcein and rhodamine-dextran were used for fluorescence visualization of the vesicle lumen.

The soluble dyes were added to the sucrose solution (0.5 mM) just before the rehydration step. Vesicle suspensions are stored in the dark at 5 °C, remaining stable for several days.

**Anti-p10 Immunofluorescence.** The membrane reconstitution of p10 protein was probed by specific immunoassay using polyclonal anti-p10 antibody (AlexaFluor488-conjugated-anti-p10-IgG expressed in rabbit). Briefly, the IgG fraction was purified from 1 mL of bulk sera, raised against purified protein p10, using a G-sepharose column affinity chromatography. Then, 1 mg of IgGs was labeled with Alexa488 using the Invitrogen kit, AlexaFluor 488 labeling kit (ref A10235). An unspecific antibody, also expressed in rabbit, was used for negative control (AlexaFluor488-conjugated-anti-x-IgG). GUVs preparations were incubated overnight with the corresponding antibody dye. Prior to microscopy observation, in order to reduce fluorescence background arising from non integrated protein, the preparation was first washed out in excess saline buffer supplemented with glucose 308 mM and then centrifuged at 10,000 rpm for 2 min (Hettich Zentrifugen, Mikro 120).

**Optical Microscopy.** For microscopy observation, freshly made GUVs prepared at different compositions were transferred to a glucose (310 mM) solution. Fluorescence images were monitored under an inverted microscope in the fluorescence mode (Nikon Eclipse TE2000; 100 W Hg lamp; FITC and Texas Red filter sets) and recorded with a cooled CCD (Nikon DS-1QM, 14 fps, 1 megapixel).

**LUVs for Confocal Microscopy.** We used a confocal microscope Leica SP2 with a DMIRE 2 stage. Two different excitation lasers were used, Ar/ArKr (488 nm) and HeNe (543 nm) for emission in the green (calcein) and red (rhodamine) channels, respectively. Images were acquired and treated using the Leica Confocal Software (LCS). Extruded LUVs were prepared through polycarbonate membranes (1  $\mu$ m pore size) following the same protocol as above. Proteo-LUVs were prepared by lipid co-extrusion (16 mg/mL total lipid) with the protein solution in saline buffer (0.1  $\mu$ g/mL protein, 50 mM Tris-HCl, pH 7.8, 200 mM NaCl) in the presence of rhodamine-dextran (0.5 mM) and calcein (0.5 mM). For control, lipid LUVs were also prepared with internalized dyes in the absence of protein. To get optical contrast between the fluorescent inner lumen and the outer suspending medium, 5  $\mu$ L of proteoliposome suspension was diluted in 15  $\mu$ L of dye-free buffer solution (50 mM TrisHCl, 200 mM NaCl) and stored at 4 °C overnight.

**Supported Planar Lipid Bilayers.** A 40  $\mu$ L portion of 0.1 g/L LUV solution in 50 mM Tris-HCl, 200 mM NaCl, 2 mM CaCl<sub>2</sub> (pH 7.8) was incubated on a freshly cleaved mica surface for 1 h, resulting in the formation of a supported lipid bilayer as described in ref 34. The solution containing the nonfused lipid vesicles was removed and replaced by working buffer. Incomplete lipid bilayers were formed by reducing to a few minutes the time the mica surface was exposed to solution containing the lipid vesicles.

**Atomic Force Microscopy.** AFM images were taken with a microscope from Nanotec Electrónica SL (Spain) operated in the jump mode.<sup>37</sup> The scanning piezo was calibrated using silicon calibration grating (NT-MDT Moscow, Russia). Silicon nitride tips (Olympus) with a force constant of 0.05 N/m were used. To observe planar lipid bilayer structures on mica, LUV solutions were incubated as described above. Excess protein was removed from solution, and excess buffer was added before imaging. This protocol resulted in reproducible interaction of

the lipid bilayer to the mica surface. To analyze AFM images we used WSXM, a free software developed by Nanotec Electrónica SL (Spain).<sup>38</sup>

## AUTHOR INFORMATION

### Corresponding Author

\*E-mail: monroy@quim.ucm.es.

### Present Address

#Agencia Española del Medicamento y Productos Sanitarios (AEMPS), Campezo 1, Edificio 8, 28022 Madrid, Spain

### Author Contributions

The manuscript was written through contributions of all authors. All authors have given approval to the final version of the manuscript.

### Funding

Ministerio de Ciencia e Innovación (MICINN) del Gobierno de España. Comunidad de Madrid (CM). Universidad Complutense de Madrid/Banco Santander Central Hispano (UCM/BSCH).

### Notes

The authors declare no competing financial interest.

## ACKNOWLEDGMENTS

We are grateful to Concepcion Revilla and Javier Dominguez (Dept. Biotecnología, INIA) for help in the preparation of fluorescently labeled antibodies. We thank Centro de Citometría-Microscopia de Fluorescencia (UCM) for confocal microscopy time and Departamento de Bioquímica y Biología Molecular I (UCM) for the use of ultracentrifuges. This work was partly financed by MICINN under grants FIS2009-16450-C02-01 (to FM), BIO2008-04478-C03 (to M.V.), BFU2011-29038-C02-1 (to J.L.C.), CONSOLIDER CSD2007-00010 (to F.M., J.L.C., and M.V.), S2009/MAT1507 from CM (to F.M., J.L.C., and M.V.), and GR35/10-B-921539 from UCM/BSCH (to F.M.).

## REFERENCES

- (1) Bustamante, C.; Bryant, Z.; and Smith, S. B. (2003) Ten years of tension: single-molecule DNA mechanics. *Nature* 421 (6921), 423–427.
- (2) Smith, D. E., Tans, S. J., Smith, S. B., Grimes, S., Anderson, D. L., and Bustamante, C. (2001) The bacteriophage [phi]29 portal motor can package DNA against a large internal force. *Nature* 413 (6857), 748–752.
- (3) Sun, S., Rao, V. B., and Rossmann, M. G. (2010) Genome packaging in viruses. *Curr. Opin. Struct. Biol.* 20 (1), 114–120.
- (4) Carrascosa, J. L. (1986) *Electron Microscopy of Proteins*, Vol. 5, p 37–70, Academic Press, New York.
- (5) Johnson, J. E. (2010) Virus particle maturation: insights into elegantly programmed nanomachines. *Curr. Opin. Struct. Biol.* 20 (2), 210–216.
- (6) Steven, A. C., Heymann, J. B., Cheng, N., Trus, B. L., and Conway, J. F. (2005) Virus maturation: dynamics and mechanism of a stabilizing structural transition that leads to infectivity. *Curr. Opin. Struct. Biol.* 15 (2), 227–236.
- (7) Valpuesta, J. M., and Carrascosa, J. L. (1994) Structure of viral connectors and their function in bacteriophage assembly and DNA packaging. *Q. Rev. Biophys.* 27 (02), 107–155.
- (8) Cuervo, A.; Carrascosa, J. L., Viral connectors for DNA encapsulation. *Curr. Opin. Biotechnol.* 2011, (0).
- (9) Wikoff, W. R., and Johnson, J. E. (1999) Virus assembly: Imaging a molecular machine. *Curr. Biol.* 9 (8), R296–R300.
- (10) Agirrezabal, X., Martin-Benito, J., Caston, J. R., Miranda, R., Valpuesta, J. M., and Carrascosa, J. L. (2005) Maturation of phage T7



involves structural modification of both shell and inner core components. *EMBO J.* 24 (21), 3820–3829.

(11) Valpuesta, J. L. C. a. J. M. (1999) Bacteriophage connectors: structural features of a DNA translocating motor. *Recent Res. Dev. Virol.* 1, 449–465.

(12) Johnson, J. E., and Chiu, W. (2007) DNA packaging and delivery machines in tailed bacteriophages. *Curr. Opin. Struct. Biol.* 17 (2), 237–243.

(13) Orlova, E. V., Gowen, B., Droge, A., Stiege, A., Weise, F., Lurz, R., van Heel, M., and Tavares, P. (2003) Structure of a viral DNA gatekeeper at 10 Å resolution by cryo-electron microscopy. *EMBO J.* 22 (6), 1255–1262.

(14) Newcomb, W. W., Juhas, R. M., Thomsen, D. R., Homa, F. L., Burch, A. D., Weller, S. K., and Brown, J. C. (2001) The UL6 gene product forms the portal for entry of DNA into the herpes simplex virus capsid. *J. Virol.* 75 (22), 10923–32.

(15) Trus, B. L., Cheng, N., Newcomb, W. W., Homa, F. L., Brown, J. C., and Steven, A. C. (2004) Structure and polymorphism of the UL6 portal protein of herpes simplex virus type 1. *J. Virol.* 78 (22), 12668–71.

(16) Chang, J., Weigele, P., King, J., Chiu, W., and Jiang, W. (2006) Cryo-EM asymmetric reconstruction of bacteriophage p22 reveals organization of its dna packaging and infecting machinery. *Structure* 14 (6), 1073–1082.

(17) Jiang, W., Chang, J., Jakana, J., Weigele, P., King, J., and Chiu, W. (2006) Structure of epsilon15 bacteriophage reveals genome organization and DNA packaging/injection apparatus. *Nature* 439 (7076), 612–616.

(18) Wendell, D., Jing, P., Geng, J., Subramaniam, V., Lee, T. J., Montemagno, C., and Guo, P. (2009) Translocation of double-stranded DNA through membrane-adapted phi29 motor protein nanopores. *Nat. Nano* 4 (11), 765–772.

(19) Jing, P., Haque, F., Vonderheide, A. P., Montemagno, C., and Guo, P. (2010) Robust properties of membrane-embedded connector channel of bacterial virus phi29 DNA packaging motor. *Mol. BioSyst.* 6 (10), 1844–1852.

(20) Jing, P., Haque, F., Shu, D., Montemagno, C., and Guo, P. (2010) One-way traffic of a viral motor channel for double-stranded DNA translocation. *Nano Lett.* 10 (9), 3620–3627.

(21) Geng, J., Fang, H., Haque, F., Zhang, L., and Guo, P. (2011) Three reversible and controllable discrete steps of channel gating of a viral DNA packaging motor. *Biomaterials* 32 (32), 8234–8242.

(22) Fang, H., Jing, P., Haque, F., and Guo, P. (2012) Role of channel lysines and the “push through a one-way valve” mechanism of the viral DNA packaging motor. *Biophys. J.* 102 (1), 127–135.

(23) Guasch, A., Pous, J., Ibarra, B., Gomis-Rüth, F. X., Valpuesta, J. M., Sousa, N., Carrascosa, J. L., and Coll, M. (2002) Detailed architecture of a DNA translocating machine: the high-resolution structure of the bacteriophage [phi]29 connector particle. *J. Mol. Biol.* 315 (4), 663–676.

(24) Valpuesta, J. M., Fernández, J. J., Carazo, J. M., and Carrascosa, J. L. (1999) The three-dimensional structure of a DNA translocating machine at 10 Å resolution. *Structure* 7 (3), 289–296.

(25) Ibanez, C., Garcia, J. A., Carrascosa, J. L., and Salas, M. (1984) Overproduction and purification of the connector protein of *Bacillus subtilis* phage phi 29. *Nucleic Acids Res.* 12 (5), 2351–2365.

(26) Davies, S. S., Pontsler, A. V., Marathe, G. K., Harrison, K. A., Murphy, R. C., Hinshaw, J. C., Prestwich, G. D., Hilaire, A. S., Prescott, S. M., Zimmerman, G. A., and McIntyre, T. M. (2001) Oxidized alkyl phospholipids are specific, high affinity peroxisome proliferator-activated receptor gamma ligands and agonists. *J. Biol. Chem.* 276, 16015–16023.

(27) Fruhwirth, G. O., Loidl, A., and Hermetter, A. (2007) Oxidized phospholipids: from molecular properties to disease. *Biochim. Biophys. Acta* 1772, 718–736. Mattila, J. P., and Kinnunen PK, S. K. (2008) Oxidized phospholipids as potential molecular targets for antimicrobial peptides. *Biochim. Biophys. Acta* 1778 (10), 2041–50.

(28) Khandelia, H., and Mouritsen, O. G. (2009) Lipid gymnastics: evidence of complete acyl chain reversal in oxidized phospholipids from molecular simulations. *Biophys. J.* 96 (7), 2734–2743.

(29) Karlsson, O., Rytömaa, M., Dahlqvist, A., Kinnunen, P. K. J., , A°., and Wieslander (1996) Correlation between bilayer lipid dynamics and activity of the diglucosyldiacylglycerol synthase from *Acholeplasma laidlawii* membranes. *Biochemistry* 35, 10094–10102.

(30) Prenner, E., Sommer, A., Maurer, N., Glatter, O., Gorges, R., Paltauf, F., and Hermetter, A. (2000) Lateral microheterogeneity of diphenylhexatriene-labeled choline phospholipids in the erythrocyte ghost membrane as determined by time-resolved fluorescence spectroscopy. *J. Membr. Biol.* 174, 237–243.

(31) Sabatini, K., Mattila, J.-P., Megli, F. M., and Kinnunen, P. K. J. (2006) Characterization of two oxidatively modified phospholipids in mixed monolayers with DPPC. *Biophys. J.* 90, 4488–4499.

(32) Boal, D. H. (2005) *Mechanics of the Cell*, 3rd ed., p xiv, Cambridge University Press, New York.

(33) Phillips, R., Ursell, T., Wiggins, P., and Sens, P. (2009) Emerging roles for lipids in shaping membrane-protein function. *Nature* 459 (7245), 379–385.

(34) Nagle, J. F., and Tristram-Nagle, S. (2000) Structure of lipid bilayers. *Biochim. Biophys. Acta* 1469, 159–195.

(35) Z. V. Leonenko, E. F., Ma, H., Dahms, T. E. S., and Cramb, D. T. (2004) Investigation of temperature-induced phase transitions in DOPC and DPPC phospholipid bilayers using temperature-controlled scanning force microscopy. *Biophys. J.* 86, 3783–3793.

(36) Richter, R., Mukhopadhyay, A., and Brisson, A. (2003) Pathways of lipid vesicle deposition on solid surfaces: a combined QCM-D and AFM study. *Biophys. J.* 85 (5), 3035–3047.

(37) Moreno-Herrero, F., de Pablo, P. J., Fernandez-Sanchez, R., Colchero, J., Gomez-Herrero, J., and Baro, A. M. (2002) Scanning force microscopy jumping and tapping modes in liquids. *Appl. Phys. Lett.* 81 (14), 2620–2622.

(38) Horcas, I., Fernandez, R., Gomez-Rodriguez, J. M., Colchero, J., Gomez-Herrero, J., and Baro, A. M. (2007) WSXM: A software for scanning probe microscopy and a tool for nanotechnology. *Rev. Sci. Instrum.* 78 (1), 013705–8.

(39) Alberts, B. (2002) *Cell Biology Interactive*, 4th ed., Garland Science, New York.

(40) Tamba, Y., Ohba, S., Kubota, M., Yoshioka, H., Yoshioka, H., and Yamazaki, M. (2007) Single GUV method reveals interaction of tea catechin (–)-epigallocatechin gallate with lipid membranes. *Biophys. J.* 92 (9), 3178–3194.

(41) Betz, W. J., Mao, F., and Smith, C. B. (1996) Imaging exocytosis and endocytosis. *Curr. Opin. Neurobiol.* 6, 365–371.

(42) Abramoff, M. D., Magalhaes, P. J., and Ram, S. J. (2004) Image processing with ImageJ. *Biophotonics Int.* 11 (7), 36–42.

(43) Brian, A. A., and McConnell, H. M. (1984) Allogeneic stimulation of cytotoxic T cells by supported planar membranes. *Proc. Natl. Acad. Sci. U.S.A.* 81, 6159–6163.

(44) Lopez-Montero, I., Arriaga, L. R., Monroy, F., Rivas, G., Tarazona, P., and Velez, M. (2008) High fluidity and soft elasticity of the inner membrane of *Escherichia coli* revealed by the surface rheology of model langmuir monolayers. *Langmuir* 24 (8), 4065–4076.